ASSIMILATION OF TOMOGRAPHIC PARTICLE IMAGE VELOCIMETRY DATA OF TURBULENT MIXED CONVECTION IN A CUBOIDAL CELL

Christian Bauer^{a,*}, Michael Mommert^a and Claus Wagner^{a,b}

^aInstitute of Aerodynamics and Flow Technology German Aerospace Center, Göttingen, Germany ^bInstitute of Thermodynamics and Fluid Mechanics Technische Universität Ilmenau, Germany

*christian.bauer@dlr.de

Keywords: tomographic particle image velocimetry, turbulent mixed convection, data assimilation, direct numerical simulation

1. INTRODUCTION

Data assimilation, i.e. the application of numerical algorithms to experimental data in order to extract additional information, has become an increasingly important topic in the field of fluid dynamics and turbulence research in the last decades (Carrassi et al. 2018, di Leoni et al. 2020). Although tomographic particle image velocimetry (tomo PIV) allows the acquisition of time-dependent, three-dimensional velocity fields of turbulent flows, it usually cannot measure all the essential parts of the flow problem. Due to the reflection of the laser light sheet and the low tracer particle densities near solid walls, it is difficult to completely capture boundary layers using PIV. In addition, small-scale turbulent structures are often filtered out, because the velocity vectors represent surface- or volume-averaged quantities obtained from a correlation step.

In addition, for fluid problems involving thermal convection, the temperature field—next to the velocity field—is essential for understanding the flow problem. However, to capture the temperature field simultaneously with the velocity field requires additional elaborate measurement techniques that are often not feasible.

Thus, Bauer et al. (2022) present an algorithm for the problem of turbulent Rayleigh–Bénard convection that allows the assimilation of tomo PIV-measured velocity fields and the construction of corresponding temperature fields without additional measurements, but solely by exploiting the governing flow equations. In the present work, we extend our data assimilation scheme to the problem of turbulent mixed convection in a cuboidal cell, where pressure-driven forces act on the flow superimposed with buoyancy.

Such mixed convection flows, which describe the phenomenon of the simultaneous occurrence of both forced and natural convection, are of great practical importance to engineering applications such as heat exchangers or air conditioning in the passenger cabins of airplanes, trains, or other vehicles.

To investigate the dynamics of turbulent mixed convection and, in particular, the dynamics of the large-scale circulation (LSC), Schmeling et al. (2013) recorded fluid temperature time series in the same cuboidal sample used in the present study. The simplified generic geometry allows for a more fundamental analysis of the flow than the aforementioned specific engineering applications, while at the same time avoiding the problems arising from complex geometries for both experimental and numerical investigations. As shown in Figure 1, the LSC in mixed convection can be decomposed into a forced convection roll and a thermal convection roll. Schmeling et al. (2013) found four different possible states of the thermal convection roll: A three-roll and a four-roll state, each of which with two different diagonal orientations.

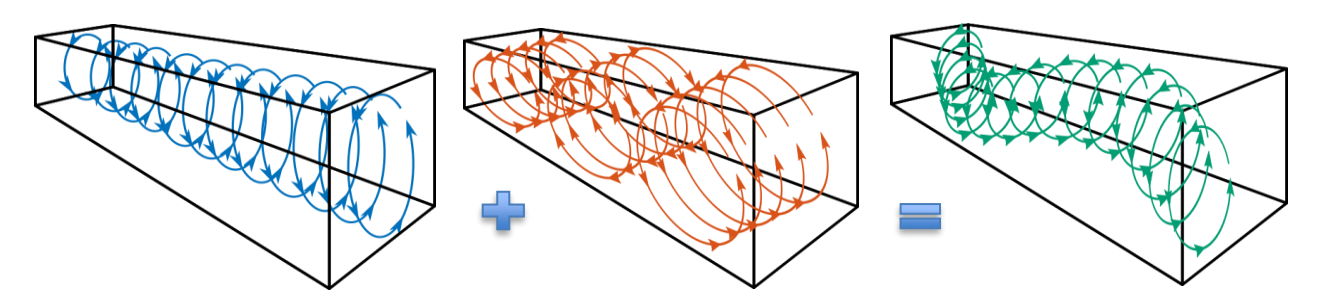


Figure 1. Sketch of the large-scale circulation in mixed convection. Left: Forced convection roll. Middle: Thermal convection roll (three-roll state). Right: Resulting large-scale ciculation.

Mommert et al. (2020) observed reconfigurations between the four- and the three-roll states using tomo PIV measurements. In the present study, we aim to assimilate the tomo PIV data for both states so as to obtain fully-resolved velocity and temperature fields. Furthermore, we use the assimilation scheme to extend the measurement data from one quarter of the complete sample of Mommert et al. (2020) to the entire sample, i.e. to regions that were not initially covered by the tomo PIV measurements.

The present study is organized as follows: In section 2, the experimental setup of the mixed convection cell measurement is depicted. Subsequently, the data assimilation algorithm applied to the measured velocity field is presented in section 3 before the results are discussed in section 4. Finally, the paper is concluded in section 5.

2. EXPERIMENTAL SET UP

The experimental data set is obtained from the tomographic PIV (tomo PIV, Kühn et al., 2011, 2012) measurement of a mixed convection cell reported by Mommert et al. (2020). The experiment consists of a rectangular sample with dimensions L_x =2500mm, L_y = L_z = \hat{H} =500mm, as shown in Figure 2.

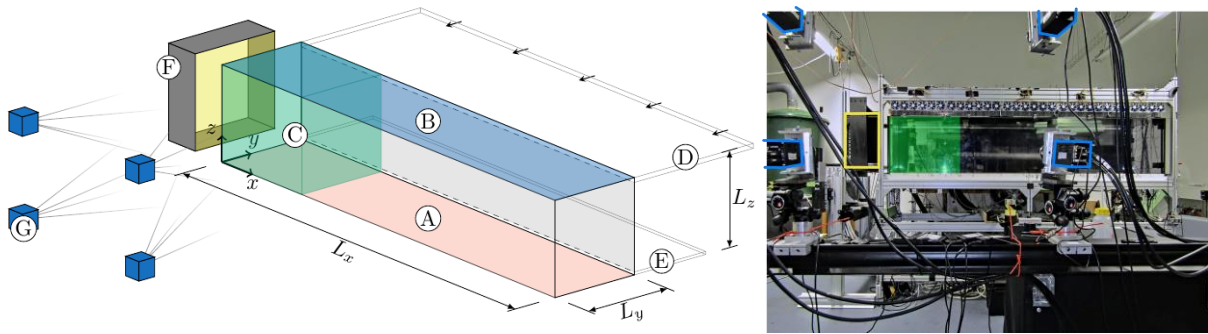


Figure 2. Left: Sketch of the mixed convection sample with heated bottom (A) and cooled top plate (B); Measurement volume (C); Velocity inlet (D) and outlet (E); LED light system (F) and PIV camera system (G). Right: Photograph of the mixed convection sample. Figure adapted from Mommert et al. (2020).

The aluminum bottom plate (A) is heated by tempered water, whereas the aluminum top plate (B) is passively cooled to room temperature. To minimize heat exchange with the surroundings while allowing optical access, the side walls of the sample are made of double-walled, 10mm-thick polycarbonate. Moreover, a 25mm high velocity inlet (D) and a 15mm high velocity outlet (E) were attached to the top and the bottom edges, respectively. The flow in a subvolume of the mixed convection cell (C) is captured by acquiring images of helium-filled soap bubbles illuminated by an LED lighting system (F) with a PIV camera system (G). For further details, the reader is referred to Mommert et al. (2020).

3. DATA ASSIMILATION SCHEME

The turbulent mixed convection flow can be characterized by the Prandtl number $\Pr = \hat{v}/\hat{\kappa}$, representing the ratio of momentum diffusivity and thermal diffusivity, the Rayleigh number $\Pr = \hat{u}_{in}\hat{H}/\hat{v}$, reflecting the ratio of buoyancy and diffusion forces, and the Reynolds number $\Pr = \hat{u}_{in}\hat{H}/\hat{v}$, representing the ratio of inertial and viscous forces, with \hat{v} the kinematic viscosity, $\hat{\kappa}$ the thermal diffusivity, $\hat{\alpha}$ the thermal expansion coefficient, \hat{g} the gravitational acceleration, \hat{H} the mixed convection cell height, $\hat{\Delta T}$ the vertical temperature difference, and \hat{u}_{in} the inlet velocity. In the following, dimensional quantities are denoted with a circumflex and the dimensionless quantities are denoted without a circumflex. The equations governing the problem are the transport equations for mass, momentum, and energy which, for an incompressible fluid and the Boussinesq approximation, are in dimensionless form

$$\nabla \cdot u = 0,$$
 (1)

$$\frac{\partial u}{\partial t} + \boldsymbol{u} \cdot \nabla \boldsymbol{u} = -\nabla p + \sqrt{\frac{P_r}{R_a}} \nabla^2 \boldsymbol{u} + T \boldsymbol{e}_{\boldsymbol{z}},\tag{2}$$

$$\frac{\partial T}{\partial t} + \mathbf{u} \cdot \nabla T = \sqrt{\frac{1}{PrRa}} \nabla^2 T,\tag{3}$$

with \mathbf{u} the velocity vector (u,v,w), p the pressure, T the temperature, and $\mathbf{e}_{\mathbf{z}}$ the unit vector in the vertical direction. In experimentally-measured data, the conservation of mass, equation (1), is often not satisfied. Therefore, we apply the following algorithm to the measured velocity fields to ensure the divergence-free condition: First, the divergence of each measured velocity field is calculated. Afterwards, a pseudo pressure field is obtained by solving the Poisson equation for the measured velocity field. Finally, the velocity field is corrected by the pseudo pressure field.

The obtained divergence-free velocity fields are then fed into a nudging algorithm, which is a further development of the algorithm we used for Rayleigh–Bénard convection (Bauer et al., 2022) and is similar to the one introduced by Suzuki and Yamamoto (2015). Starting from an initial velocity and temperature field provided by a direct numerical simulation (DNS) conducted for the characteristic dimensionless numbers of the experiment Ra=1.4×10⁸, Re=7350, and Pr=0.7 for air, the governing equations (1-3) are integrated in time with the momentum equation being expanded by a feedback term that penalizes the deviation of the computed velocity from the experimentally-obtained, divergence-free velocity field, viz.

$$\frac{\partial u}{\partial t} + \mathbf{u} \cdot \nabla \mathbf{u} = -\nabla p + \sqrt{\frac{Pr}{Ra}} \nabla^2 \mathbf{u} + T \mathbf{e}_z + \alpha (\mathbf{u}_{ref} - \mathbf{u}), \tag{4}$$

where α is the feedback gain and u_{ref} represents the experimentally-obtained, divergence-free velocity field linearly interpolated between two consecutive snapshots. A schematic sketch of the algorithm is depicted in Figure 3. In the subvolume of the mixed convection sample where tomo PIV velocity data were acquired (green volume in Figure 2), the time-integrated velocity field is subjected to a force at each time step that is proportional to the deviation of the velocity field from the corresponding tomo PIV velocity field. Thus, after an initial transient phase, the simulated flow field evolves towards the measured one in the measurement subvolume, while its extension in the rest of the sample evolves according to the conservation of mass, momentum, and energy (equations 1-3). As a consequence, the flow field becomes accessible not only in the measurement volume, but also in the rest of the sample as well as in the boundary layers in the vicinity of solid walls, which were not initially captured. In addition, the temperature field, which corresponds to the simulated velocity field and thus to the measured velocity field, becomes accessible.

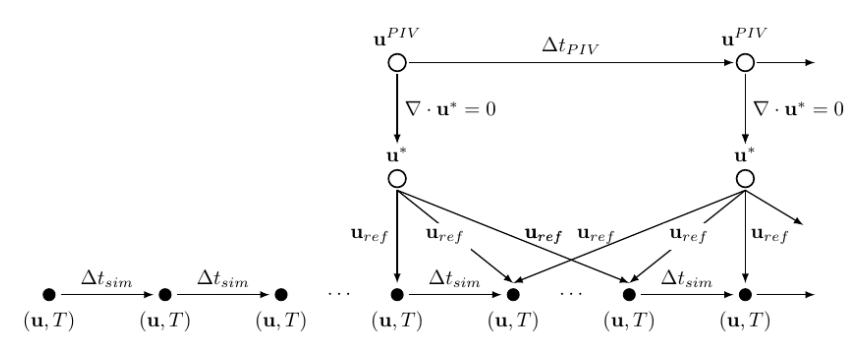


Figure 3. Schematic sketch of the nudging algorithm. u, time-integrated velocity; T, time-integrated temperature; \mathbf{u}^{PIV} , tomo PIV-measured velocity; \mathbf{u}^* , divergence-free velocity for each tomo PIV snapshot; \mathbf{u}_{ref} , linearly interpolated velocity at every time step from consecutive PIV snapshots; Δt_{sim} , simulation time step; Δt_{PIV} , tomo PIV time step.

As reported by Mommert et al. (2022), the time scale for reconfiguration events in the considered mixed convection cell is of the order of hours. Hence, due to the computational resources required to capture such large time scales, it does not seem feasible to capture a reconfiguration event with a conventional DNS without nudging. Moreover, the conditions that could favor a reconfiguration event in the laboratory environment may not be present in the DNS, where perfectly adiabatic sidewalls, isothermal heating and cooling plates, as well as smooth walls are considered as boundary conditions. Nevertheless, with the present hybrid PIV/DNS approach, our first goal is to reproduce two different states in a statistically quasi-stationary form. Therefore, we set up two different simulation cases—shown in Table 1—where the initial PIV fields correspond to one of the two states, while the initial DNS field is a fully developed turbulent mixed convection computed without nudging. Note that the numerical grid is refined toward the solid walls in order to resolve the steep velocity and temperature gradients as well as the smallest scales of turbulent motions, which is the Kolmogorov scale for the velocity field and the Batchelor scale for the temperature field, respectively.

Table 1. Simulation cases. Pr and Ra are the Prandtl and the Rayleigh number, respectively. α is the feedback gain. N_x , N_y , N_z are the number of grid points in the corresponding direction. $\Delta i_{min}/H$, $\Delta i_{max}/H$ are the minimum and maximum grid spacings in i direction (i=x,y,z), respectively. \hat{t}_{ini}^{PIV} is the time of the initial PIV snapshot.

Case	$\hat{\mathbf{t}}_{\mathrm{ini}}^{\mathrm{PIV}}$	Pr	Ra	Re	α	N _x	N _y	N_z	$\Delta i_{min}/H$	$\Delta i_{max}/H$
A	18153s	0.7	1.4×10 ⁸	7350	1	382	634	670	4.5×10 ⁻⁴	1.0×10 ⁻³
В	15995s									

4. RESULTS

Divergence-free condition

As described in section 3, the measured tomo PIV velocity fields are made divergence-free by the algorithm introduced by Bauer et al. (2022) before they are fed into the nudging algorithm as \mathbf{u}_{ref} . Figure 4 portrays the velocity component v in an xy-plane at z/H=0.5 before (a) and after the divergence has been removed (b) as well as the divergence of the measured velocity field (c).

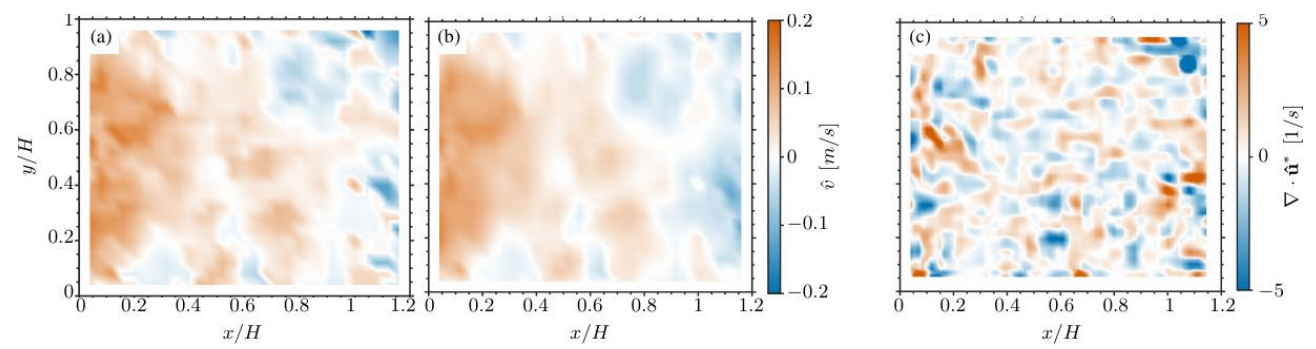


Figure 4. The velocity component v before (a) and after (b) divergence has been removed in an xy-plane at z/h=0.5. (c) The divergence of the initial tomo PIV measured velocity field.

As Figure 4 indicates, our algorithm successfully removes discontinuities from the measured velocity data by imposing the divergence-free condition.

Nudging correlation

In order to monitor the nudging of the velocity field u towards the divergence-free measured velocity field u_{ref} , the correlation coefficient is calculated as follows:

$$C_{u_i u_{ref,i}} = \frac{cov(u_i u_{ref,i})}{RMS(u_i)RMS(u_{ref,i})},\tag{5}$$

with

$$COV(u_{i}, u_{ref,i}) = \int_{z=0}^{H} \int_{y=0}^{H} \int_{x=0}^{L} (u_{i} - \langle u_{i} \rangle_{xyz}) (u_{ref,i} - \langle u_{ref,i} \rangle_{xyz}) dxdydz$$
 (6)

and

$$RMS(u_i) = \sqrt{\int_{z=0}^{H} \int_{y=0}^{H} \int_{x=0}^{1.2H} (u_i - \langle u_i \rangle_{xyz})^2 dx dy dz}.$$
 (7)

Accordingly, the temporal evolution of the correlation coefficient of the three velocity components is presented in Figure 5. All the three components reach correlation coefficients of more than 0.98 for case A and 0.97 for case B within 2 dimensionless time units after the initialization of the simulation. Thus, the solver quickly adapts to the feedback term that imposes the PIV-measured velocity field. It should be noted that in both cases, the ν -component has the highest correlation coefficient ($C_{\nu\nu_{ref}} > 0.99$). Additionally, for case B the ν -component, which contributes only to the thermal

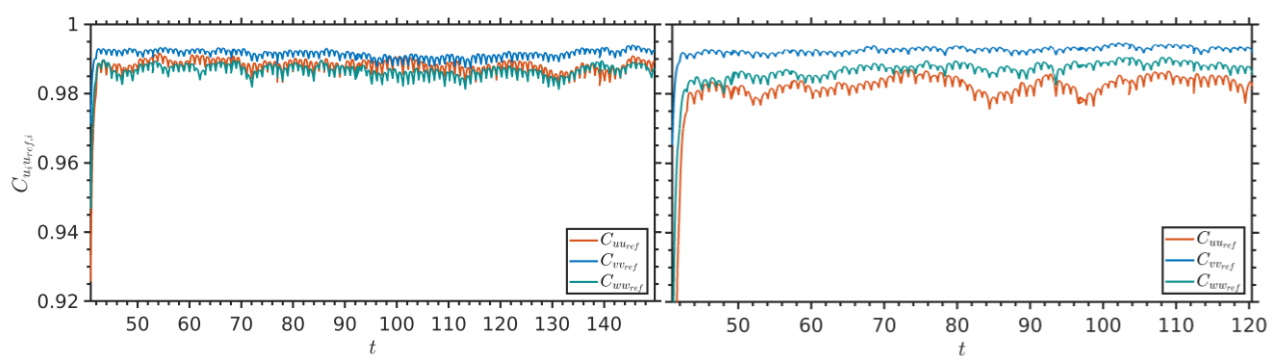


Figure 5. Correlation coefficients $C_{u_iu_{ref,i}}$ of the i-component of the simulated velocity field u_i and the divergence-free PIV field $u_{ref,i}$ for case A (left) and case B (right).

but not to the forced convection roll, cf. Figure 1, shows the lowest correlation between the simulated and the measured velocity. The fact that the correlation coefficients corresponding to the convection roll are lower in case B than in case A gives a first hint that the nudging is working against a potential well, i.e. the energetically favorable state of the initial DNS flow field.

Assimilated flow fields

For case A, the hybrid PIV/DNS simulation was initialized with the DNS velocity and temperature field at t=40.94 dimensionless time units and the PIV velocity field at $\hat{t}=18153s$, the latter corresponding to the four-convective-rolls state with hot spots at one quarter and three quarter of the cell. Bear in mind that, hereinafter, the time t refers to the DNS time frame, normalized by the free-fall velocity $u_{ff} = \sqrt{\alpha \hat{g} \hat{H} \Delta \hat{T}}$ and the cell height \hat{H} . The dimensionless time between two adjacent PIV snapshots is $\Delta t_{PIV} = 1.089$. Figure 6 demonstrates the divergence-free PIV field (top) together with the corresponding simulated field (bottom) at t=124.

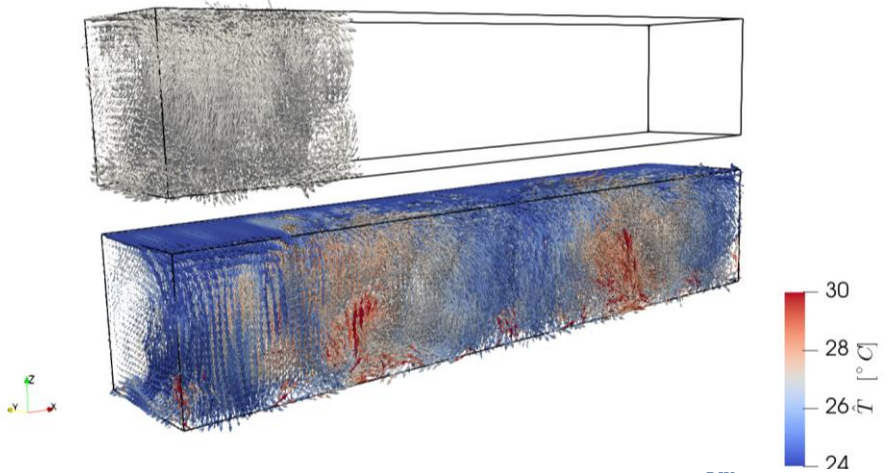


Figure 6. Instantaneous snapshots at t=124. Top: PIV velocity vector field \mathbf{u}^{PIV} . Bottom: Simulated velocity vector field \mathbf{u} (downsampled on the PIV grid). Coloring corresponds to the temperature field T.

Whereas the PIV measurement covers only approximately a quarter of the cell, the simulated field covers the entire domain. Besides, the temperature field becomes accessible in the measured subvolume as well as in the rest of the cell (Figure 6 bottom). In addition to the dominant forced convective roll, two upward thermal plumes are visible at $x/H \approx 1.25$ and $x/H \approx 3.75$, respectively. Note that in the subvolume where the PIV data were assimilated, small scales—that are absent in the PIV data set— are also suppressed in the hybrid simulation. To visualize the thermal convection roll, the time-averaged velocity field $\langle u \rangle_t$ in an xz-plane at y/H = 0.5 is presented in Figure 7. Here, the in-plane velocity components $\langle u_{xz} \rangle_t = (\langle u \rangle_t, \langle w \rangle_t)$, represented by the vector field, correspond to the thermal convection rolls, whereas the out-of-plane velocity component $\langle v \rangle_t$, represented by the pseudo-color field, corresponds to the forced convection roll. The vector field in Figure 7 clearly shows the four-roll state of the thermal convection, with the location of the upward motion coinciding with the hot thermal plumes visible in the instantaneous three-dimensional flow field in Figure 6.

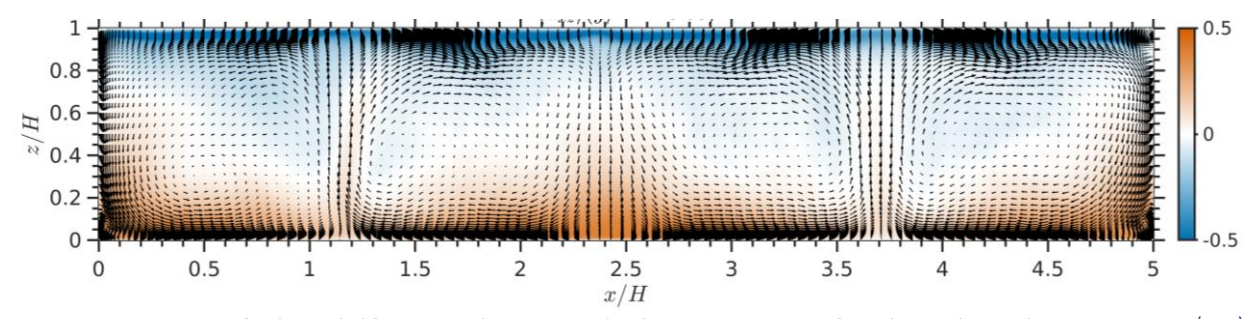


Figure 7. Time-averaged velocity field in an xz-plane at y/H=0.5 for case A. Vectors show the in-plane velocity component $\langle \mathbf{u}_{xz} \rangle_t = (\langle \mathbf{u} \rangle_t, \langle \mathbf{w} \rangle_t)$, the pseudo-color image represents the out-of-plane velocity component $\langle \mathbf{v} \rangle_t$. Averaging interval: $\Delta t = 56$.

Case B was initialized with the DNS velocity and temperature field at t = 40.94 dimensionless time units same as case A, while the PIV velocity field time series started at $\hat{t} = 15995s$, the latter corresponding to the inverse four-convective-rolls state with hot spots in the corners and the center of the cell (in x-direction). Figure 8 depicts the time-

averaged velocity field for case B in the same frame as that for case A in Figure 7. Unlike case A, case B does not feature a clear four-roll state. While the strong upward motion at $x/H \approx 3.75$ persists for case B—as for case A—there is no such plume visible at $x/H \approx 1.25$.

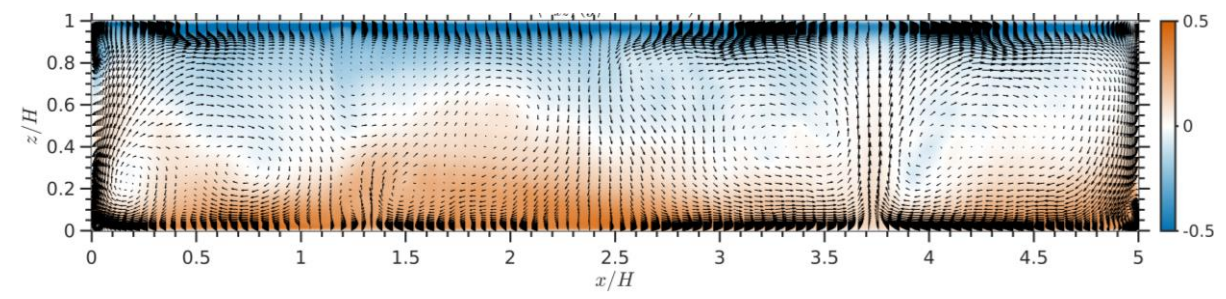


Figure 8. Time-averaged velocity field in an xz-plane at y/H=0.5 for case B. Vectors show the in-plane velocity component $\langle \mathbf{u}_{xz} \rangle_t = (\langle \mathbf{u} \rangle_t, \langle \mathbf{w} \rangle_t)$, the pseudo-color image represents the out-of-plane velocity component $\langle \mathbf{v} \rangle_t$. Averaging interval: $\Delta t = 28$.

A good measure to compare the convection roll state between case A and case B is the two-dimensional stream function of the time-averaged in-plane velocity components in the xz-plane at y/H=0.5 or in the xy-plane at z/H=0.5,

$$\psi_{\langle u\rangle_t\langle w\rangle_t}(x,z) = \int_{\hat{x}=0}^x \langle w\rangle_t(\hat{x},z) \, d\hat{x} - \int_{\hat{x}=0}^z \langle u\rangle_t(x,\hat{x}) \, d\hat{x},\tag{8}$$

$$\psi_{\langle u\rangle_t\langle v\rangle_t}(x,y) = \int_{\hat{x}=0}^x \langle v\rangle_t(\hat{x},y) \, d\hat{x} - \int_{\hat{v}=0}^y \langle u\rangle_t(x,\hat{y}) \, d\hat{y}. \tag{9}$$

Accordingly, iso-contours of the time-averaged in-plane velocities are portrayed in Figure 9 for the xz-plane at y/H=0.5 and in Figure 11 for the xy-plane at z/H=0.5.

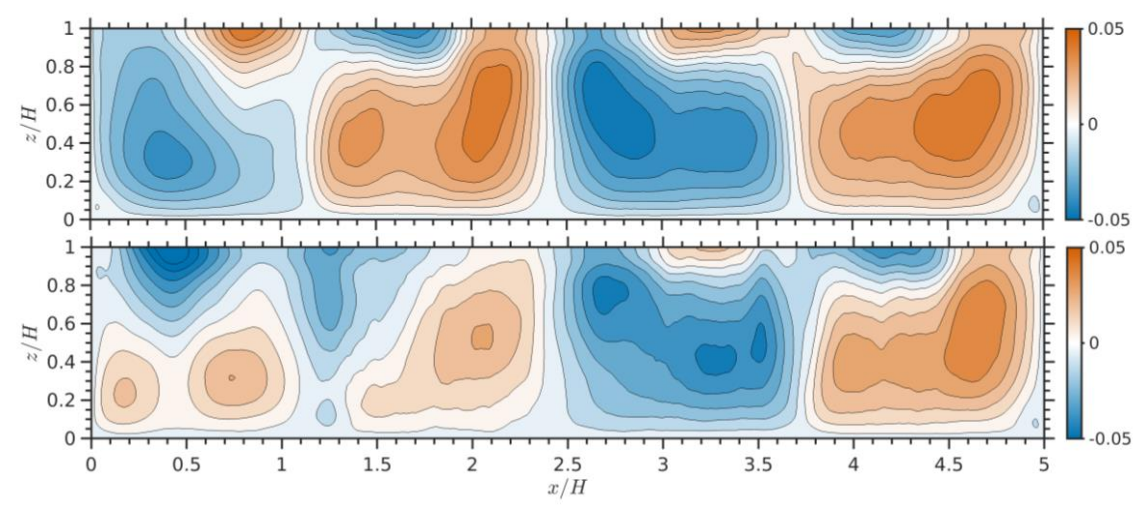


Figure 9. Iso-contours of the stream function of the time-averaged in-plane velocity components $\psi_{\langle u \rangle_t,\langle w \rangle_t}$ in an xz-plane at y/H=0.5. Top, case A; Bottom, case B.

While for case A (Figure 9, top) a four-roll state is clearly visible in the form of two pairs of counter-rotating rolls, the picture seems less clear for case B shown in Figure 9 (bottom). For case B between $2.5 \le x/H \le 5$ the two counter-rotating rolls are aligned similarly to case A, whereas between $0 \le x/H \le 2.5$ the rolls are less coherent and presumably emerging into one large clockwise-rotating roll. The latter becomes clearer when considering the stream function iso-contours of the stream function in the xy-plane at z/H = 0.5 in Figure 11, where a four-roll state is visible for case A (top) and a three-roll state for case B (bottom).

Let us focus on the temporal evolution of the different states in terms of w-profile along the x-direction at y/H = 0.5, z/H = 0.5, see Figure 10. For case A (Figure 10, left), the two upward plumes reflect in positive iso-contour values of similar intensity at locations $x/H \approx 1.25$ and $x/H \approx 3.75$ constant in time. For case B (Figure 10, right), on the other hand, three upward plumes manifest: The first at $x/H \approx 0$ constant in time and weaker in intensity than the plumes of case A; The second at location $x/H \approx 1.25$ at the beginning of the simulation (t = 40.94) then slowly drifting towards $x/H \approx 1.5$ (t = 120) while loosing intensity; The third at the location $x/H \approx 3.75$ constant in time and similar to the one of case A. The slow drift of the x-location of the second plume in case B might be an indicator, that although the flow

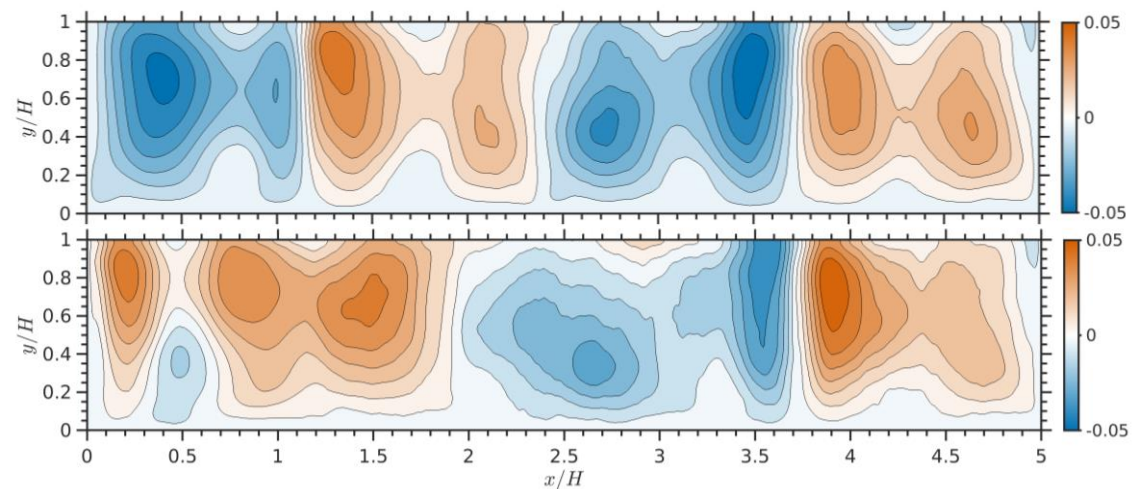


Figure 11. Iso-contours of the stream function of the time-averaged in-plane velocity components $\psi_{\langle u \rangle_t,\langle v \rangle_t}$ in an xy-plane at z/H=0.5. Top, case A; Bottom, case B.

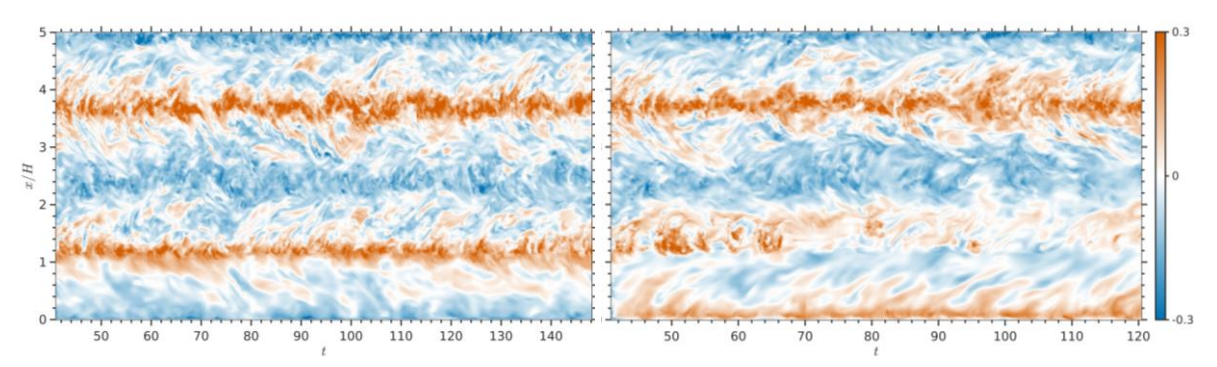


Figure 10. Temporal evolution of the w velocity component at y/H = 0.5, z/H = 0.5 along the x-direction. Left, Case A; Right, Case B.

adapts to the PIV field within the first two dimensionless time units, much more time is required for the transition to the inverse four-roll state. The simulation time of case B covers approximately 80 dimensionless time units which corresponds to 87.2s, and is at least one order of magnitude smaller than the duration of a reconfiguration event. In agreement with the experiment reported in Mommert et al. (2022), the transition from one four-roll state to another four-roll state occurs via a three-roll state persisting several hundred dimensionless time units.

Heat fluxes

An important aspect of turbulent mixed convection is the distribution of heat by convective heat fluxes. The contributions to the latter can be derived from the temperature and velocity fields and are usually decomposed into the convective heat flux of the mean field and the turbulent heat flux, viz. $\langle u_i T \rangle = \langle u_i \rangle \langle T \rangle + \langle u_i' T' \rangle$. Thus, to gain insight into the dynamics of the convective heat distribution for both the three- and the four-rolls state, the vertical convective heat flux of the time-averaged velocity and temperature field $\langle w \rangle_t \langle T \rangle_t$ at y/H = 0.5 is shown in Figure 12 for case A (top) and case B (bottom). Note that the mean temperature in Figure 12 is centered around 0.5 instead of 0. Therefore, the temperature range is shifted from (-0.5,0.) to (0,1), which makes the convective heat flux more accessible because the temperature contributes only to the intensity of the heat flux while the velocity contributes to both intensity and sign. For case A in Figure 12 (top), two mushroom-like structures around $x/H \approx 1.25$ and $x/H \approx 3.75$ of intense positive heat flux correspond to the two hot thermal plumes ascending from the heated bottom plate. For case B in Figure 12 (bottom), the thermal plume at $x/H \approx 3.75$ is comparable to case A, whereas in the left half of the cell two plume-like structures appear at $x/H \approx 0$ and $x/H \approx 1.4$, both of which are weaker in intensity than the plumes in case A. These observations of the structure of the mean heat flux $\langle w \rangle_t \langle T \rangle_t$ in Figure 12 agree with the instantaneous vertical velocity in Figure 10, both serving as indicators of the x-location of thermal plumes. These thermal plumes are also reflected in the time-averaged vertical turbulent heat flux $\langle w'T' \rangle_t$ at y/H = 0.5, shown in Figure 13 for case A (top) and case B (bottom).

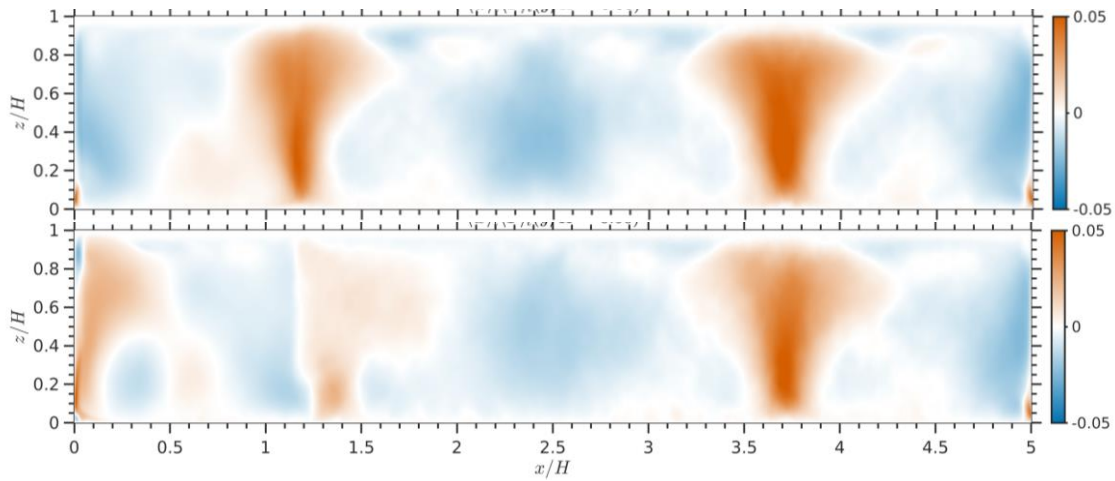


Figure 13. Vertical convective heat flux of the mean field $\langle w \rangle_t \langle T \rangle_t$ at y/H=0.5. Top, case A; Bottom, case B.

Figure 13 indicates that the average heat transport due to small-scale turbulent fluctuations is maximum near the heating and cooling plates, particularly in regions where the mean thermal plumes emerge or dissolve (cf. Figure 12), for both case A (Figure 13, top) and case B (Figure 13, bottom). Moreover, for both cases the turbulent heat flux intensity in the subvolume where the PIV fields are imposed is smaller than in the rest of the domain which is due to the suppression of the small scales by the nudging, a fact also visible in the instantaneous flow field, cf. Figure 6. For case B the turbulent heat flux intensity around $x/H \approx 1.5$, $z/H \approx 0.9$ is lower than for case A, which is consistent with the less intense mean heat flux in case B compared to case A (Figure 12, bottom).

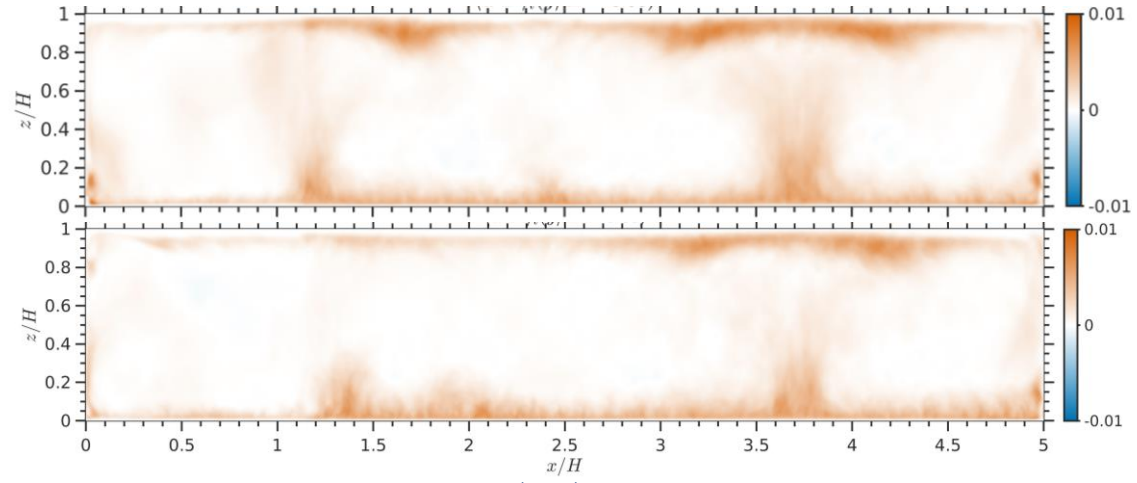


Figure 12. Time-averaged vertical turbulent heat flux $\langle w'T' \rangle_t$ at y/H=0.5. Top, case A; bottom, case B.

5. CONCLUSIONS

In order to extract additional information from tomo PIV measured velocity fields of turbulent mixed convection as well as to extend the measurement domain, we adapted our data assimilation scheme (Bauer et al., 2022), considering the governing equations of the problem. The divergence-free condition is satisfied by solving the Poisson equation for the experimentally-measured velocity field and by correcting the fields according to a fractional step method (see Figure 4). By applying a hybrid DNS/PIV approach based on the nudging algorithm outlined in Bauer et al (2022), we also extend the measured velocity field to the flow region where no data were measured. In this way, we not only improve the quality of the velocity measurement by making it divergence-free, but we also assess parameters that are not directly measured—such as the pressure and the temperature—and also expand them into regions that were not accessible by the measurement. Using a feedback gain $\alpha=1$, the flow field adapts to the imposed PIV data within 2 dimensionless time units, and the simulated flow field remains well correlated with the PIV field throughout the entire time of the hybrid simulation ($C_{u_iu_{i,ref}}>0.97$). The present method is applied to assimilate two different four-roll configurations of the thermal convection roll. However, while the four-roll state with hot spots at one quarter and three quarter of the cell is well captured in the instantaneous velocity and temperature fields as well as in the time-averaged data of case A, the inverse four roll case is not fully captured in case B. Although the reconfiguration towards the inverse four-roll state is triggered in case B, this state is not reached within the simulated time frame. Instead, a three-roll state appears in case B,

which is in good agreement with the experiment of Mommert et al. (2022), who reported long-lasting three-roll states in the transition from one four-roll state to another. In summary, the hybrid DNS/PIV approach is able to extend the flow field where the flow state of the initial DNS field matches the state of the PIV fields, but also to induce a reconfiguration event where the PIV fields contain a different flow state than the initial DNS field. In the future, the latter approach will be used to further investigate the reconfiguration in turbulent mixed convection using only DNS after the reconfiguration has been induced by the hybrid approach.

6. REFERENCES

- Bauer, C., Schiepel, D. and Wagner, C., 2022. "Assimilation and extension of particle image velocimetry data of turbulent Rayleigh–Bénard convection using direct numerical simulations". *Experiments in Fluids*, Vol. 63(22), pp. 1-17.
- Carrassi A., Bocquet M., Bertino L., Evensen G., 2018. "Data assimilation in geosciences: An overview of methods, issues, and perspectives". WIREs Climate Change, Vol. 9(5), e535.
- Di Leoni, P.C., Mazzino, A. and Biferale, L., 2020. "Synchronization to big data: Nudging the Navier-Stokes equations for data assimilation of turbulent flows". *Physical Review X*, Vol. 10(1), 011023.
- Kühn, M., Ehrenfried, K., Bosbach, J. and Wagner, C., 2011. "Large-scale tomographic particle image velocimetry using helium-filled soap bubbles". *Experiments in Fluids*, Vol. 50, pp. 929-948.
- Kühn, M., Ehrenfried, K., Bosbach, J. and Wagner, C., 2012. "Large-scale tomographic PIV in forced and mixed convection using a parallel SMART version". *Experiments in Fluids*, Vol. 53, pp. 91-103.
- Mommert, M., Schiepel, D., Schmeling, D. and Wagner, C., 2020. "Reversals of coherent structures in turbulent mixed convection". *Journal of Fluid Mechanics*, Vol. 904, A33.
- Mommert, M., 2022. "Untersuchung der Zirkulationsbewegung und des Wärmetransports in turbulenter Mischkonvektion mittels optischer Messverfahren". Dissertation. TU Ilmenau
- Schiepel, D., Schmeling, D. and Wagner, C., 2021. "Simultaneous tomographic particle image velocimetry and thermometry of turbulent Rayleigh–Bénard convection". *Measurement Sciences and Technology*, Vol. 32(9), 095201.
- Schmeling, D., Bosbach, J. and Wagner, C., 2013. "Oscillations of the large-scale circulation in turbulent mixed convection in a closed rectangular cavity". *Experiments in Fluids*, Vol. 54(5), 1517
- Suzuki, T. and Yamamoto, F., 2015. "Hierarchy of hybrid unsteady flow simulations integrating time-resolved PTV with DNS and their data-assimilation capabilities". *Fluid Dynamics Research*, Vol 47(5), 051407.